Supporting Information

Lead-Free Layered Aurivillius-Type Sn-based Halide Perovskite Ba$_2$X$_2$[Cs$_{n-1}$Sn$_n$X$_{3n+1}$] (X=I/Br/Cl) with Optimal Band Gap ~1.26 eV and Theoretical Efficiency beyond 27% for Photovoltaics

Shi-ming Liu,[a] Hong-xia Zhong,*[b] Jun-jie Liang,[c] Min Zhang,*[d] Yao-hui Zhu,[e] Juan Du,[a] Wen-hui Guo,[a] Yong He,[a] Xinqiang Wang[a] and Jun-jie Shi*[a]

[a] State Key Laboratory for Artificial Microstructures and Mesoscopic Physics, School of Physics, Peking University, Beijing 100871, China. E-mail: jjshi@pku.edu.cn
[b] School of Mathematics and Physics, China University of Geosciences, Wuhan 430074, China. E-mail: zhonghongxia@cug.edu.cn
[c] International Center for Quantum Materials, Peking University, Beijing 100871, China.
[d] Inner Mongolia Key Laboratory for Physics and Chemistry of Functional Materials, College of Physics and Electronic Information, Inner Mongolia Normal University, Hohhot 010022, China. E-mail: zhangm@imnu.edu.cn
[e] Physics Department, Beijing Technology and Business University, Beijing 100048, China.

1 Calculation method

1.1 DFT and HSE06 Calculations

The main calculations were carried out based on the Density Functional Theory (DFT) as implemented in the Vienna Ab Initio Simulation Package (VASP).[1,2] The electron-ion potential is described by the projector augmented wave (PAW) method.[3] The generalized gradient approximation (GGA) with the Perdew-Burke-Ernzerhof (PBE) are used to approximate the electron exchange and correlation potentials.[4] A 11 × 11 × 5 Monkhorst-Pack k-point mesh[5] is employed to sample the Brillouin zone for self-consistent calculation. The kinetic energy cutoff is set to 520 eV during all calculations. The convergence tolerances of the energy and force are smaller than 0.01 eV/Å and 10^{-5} eV. Considering that the normal DFT-PBE calculations usually underestimate the band gap of semiconductors seriously, we revise the band gap of Ba$_2$X$_2$[Cs$_{n-1}$Sn$_n$X$_{3n+1}$] (X=I, Br, Cl) by using the HSE06 method method (a mixture of 0.25 Hartree-Fork exchange and 0.75 PBE exchange functional)[6].

1.2 Effective Hamiltonians Built by the $k \cdot p$ Method

The Hamiltonians near the band edge are given here by the $k \cdot p$ method, in which the wave function at k is expressed as $\phi_{nk} = e^{ik \cdot r} u_n(r)$ with $u_n(r)$ derived from the basis function of $|S\rangle$, $|X\rangle$, $|Y\rangle$ and $|Z\rangle$ at the S point. The Hamiltonian matrix elements of the $k \cdot p$ model can be written as $H_{nm} = [E_{n0} + \frac{\hbar^2 k^2}{2m_0}]\delta_{nm} + \frac{\hbar}{m}k \cdot p$, where E_{n0} is the energy eigenvalue of nth state at S point, $p = -i\hbar\triangledown$ is the momentum operator.

The Hamiltonian without the SOC effect in the neighborhood of S (0.5, 0.5, 0) obtained by the $k \cdot p$ method is as follows,

$$H = \frac{\hbar^2(k^2 - k_0^2)}{2m} + \begin{bmatrix} E_{vbm,0} & P_x k_x & P_y k_y & P_z k_z \\ P_x k_x & E_{cbm,0} + L_1 k_x^2 + M_1 k_z^2 + N_1 k_y^2 & K_{xy} k_x k_y & K_{xz} k_x k_z \\ P_y k_y & K_{xy} k_x k_y & E_{cbm+1,0} + L_1 k_y^2 + M_1 k_z^2 + N_1 k_x^2 & K_{yz} k_y k_z \\ P_z k_z & K_{xz} k_x k_z & K_{yz} k_y k_z & E_{cbm+2,0} + L_2 k_z^2 + M_2(k_x^2 + k_y^2) \end{bmatrix}, \tag{S1}$$

where $E_{vbm,0}$ is energy of VBM, $E_{cbm,0}$, $E_{cbm+1,0}$ and $E_{cbm+2,0}$ are the energies of $|X\rangle$, $|Y\rangle$ and $|Z\rangle$ at S (0.5, 0.5, 0) point, K_{xy}, K_{yz}, K_{xz}, L_i, M_i and N_i are parameters due to the interaction between the conduction bands with far bands other than the valence band, P_x, P_y and P_z are parameters of the $k \cdot p$ Hamiltonian.[7]

The matrix of the SOC effect, H_{SOC} is the following expression:

$$H_{SOC} = \frac{\lambda}{2} \begin{bmatrix} 0 & -i & 0 & 0 & 0 & 1 \\ i & 0 & 0 & 0 & 0 & -i \\ 0 & 0 & 0 & -1 & i & 0 \\ 0 & 0 & -1 & 0 & i & 0 \\ 0 & 0 & -i & -i & 0 & 0 \\ 1 & i & 0 & 0 & 0 & 0 \end{bmatrix}. \tag{S2}$$

The Hamiltonian including the SOC effect at S (0.5, 0.5, 0) is the following expression:

$$H_{full} = \begin{bmatrix} E_{vbm}^* & 0 & 0 & 0 & 0 & 0 & 0 & 0 \\ 0 & E_{cbm}^* & -\lambda/2i & 0 & 0 & 0 & 0 & \lambda/2 \\ 0 & \lambda/2i & E_{cbm+1}^* & 0 & 0 & 0 & 0 & -\lambda/2i \\ 0 & 0 & 0 & E_{cbm+2}^* & 0 & -\lambda/2 & \lambda/2i & 0 \\ 0 & 0 & 0 & 0 & E_{vbm} & 0 & 0 & 0 \\ 0 & 0 & 0 & -\lambda/2 & 0 & E_{cbm}^* & \lambda/2i & 0 \\ 0 & 0 & 0 & -\lambda/2i & 0 & -\lambda/2i & E_{cbm+1}^* & 0 \\ 0 & \lambda/2 & \lambda/2i & 0 & 0 & 0 & 0 & E_{cbm+2}^* \end{bmatrix}, \tag{S3}$$

where $E_{vbm}^* = E_{vbm,0}$, $E_{cbm}^* = E_{cbm,0} + L_1 k_x^2 + M_1 k_z^2 + N_1 k_y^2$, $E_{cbm+1}^* = E_{cbm+1,0} + L_1 k_y^2 + M_1 k_z^2 + N_1 k_x^2$ and $E_{cbm+2}^* = E_{cbm+2,0} + L_2 k_z^2 + M_2(k_x^2 + k_y^2)$.

The Hamiltonian including the SOC effect along the path S (0.5, 0.5, 0) → Γ (0, 0, 0) is the following expression:

$$H_{full} = \frac{\hbar^2(k^2 - k_0^2)}{2m} + \begin{bmatrix} E_{vbm}^* & P_x k_x & 0 & 0 & 0 & 0 & 0 & 0 \\ P_x k_x & E_{cbm}^* & -\lambda/2i & 0 & 0 & 0 & 0 & \lambda/2 \\ 0 & \lambda/2i & E_{cbm+1}^* & 0 & 0 & 0 & 0 & -\lambda/2i \\ 0 & 0 & 0 & E_{cbm+2}^* & 0 & -\lambda/2 & \lambda/2i & 0 \\ 0 & 0 & 0 & 0 & E_{vbm} & P_x k_x & 0 & 0 \\ 0 & 0 & 0 & -\lambda/2 & P_x k_x & E_{cbm}^* & \lambda/2i & 0 \\ 0 & 0 & 0 & -\lambda/2i & 0 & -\lambda/2i & E_{cbm+1}^* & 0 \\ 0 & \lambda/2 & \lambda/2i & 0 & 0 & 0 & 0 & E_{cbm+2}^* \end{bmatrix}. \tag{S4}$$

1.3 Carrier Mobility

The carrier mobility μ can demonstrate the electronic transport properties more intuitively, therefore, we used the Feynman equation[8,9] to describe μ, which will be much more accurate than the deformation-potential theory because optical phonons are taken into account.[10] In room temperature, the μ can be described by the following expression,[11]

$$\mu = \frac{3\sqrt{\pi}e}{2\pi c \omega_{LO} m^* \alpha} \frac{sinh(\beta/2)}{\beta^{3/2}} \frac{w^3}{v^3} \frac{1}{K}, \tag{S5}$$

where ω_{LO} is the longitudinal optical phonon frequency, which can be calculated by the VASP code, $\beta = hc\omega_{LO}/k_BT$, v and w are variational parameters depending on temperature T, meanwhile, K is a function of v and w.[11] In this work, we obtain v and w by minimizing the free polaron energy.[11] The parameter α is electron-phonon coupling constant, introduced by Fröhlich in order to describe the movement of electrons in a polar crystal.[12] The specific expression of α is,[11]

$$\alpha = \frac{1}{\varepsilon^*} \sqrt{\frac{R_y}{ch\omega_{LO}}} \sqrt{\frac{m^*}{m_e}}, \tag{S6}$$

where R_y and m_e are the Rydberg constant and mass of electron, respectively. The ionic screening parameter, $\frac{1}{\varepsilon^*} = \frac{1}{\varepsilon_\infty} - \frac{1}{\varepsilon_{static}}$ can be calculated by the VASP code.

1.4 Interband Optical Absorption

To obtain the optical absorption coefficient, we first calculate the frequency-dependent dielectric function. The imaginary part of the dielectric function can be described as follows,[13]

$$\varepsilon_{\alpha\beta}^{(2)}(\omega) = \frac{4\pi^2 e^2}{\Omega} \lim_{q \to 0} \frac{1}{q^2} \sum_{c,v,k} 2\omega_k \delta(\varepsilon_{ck} - \varepsilon_{vk} - \omega) \times \langle u_{ck+e_\alpha q} | u_{vk} \rangle \langle u_{ck+e_\beta q} | u_{vk} \rangle^*, \tag{S7}$$

where Ω denotes the volume of the supercell, q represents the wavenumber of the incident electromagnetic wave, e_α is the unit vector in the α direction, and c and v label the conduction and valence bands, respectively. We can derive the real part of the dielectric function according to Kramers-Kronig transformation,[14]

$$\varepsilon_{\alpha\beta}^{(1)}(\omega) = 1 + \frac{2}{\pi} P \int_0^\infty \frac{\varepsilon_{\alpha\beta}^{(2)}(\omega')\omega'}{\omega'^2 - \omega^2 + i\eta} d\omega', \tag{S8}$$

where P represents the principle value. The absorption coefficient $\alpha(\omega)$ can thus be calculated by the following expression,[15]

$$\alpha(\omega) = \sqrt{2}\omega[\sqrt{\varepsilon^{(1)}(\omega)^2 + \varepsilon^{(2)}(\omega)^2} - \varepsilon^{(1)}(\omega)]^{1/2}. \tag{S9}$$

1.5 Spectroscopic Limited Maximum Efficiency (SLME)

The theoretical maximum solar cell efficiency is defined as

$$\eta = \frac{P_m}{P_{in}}, \tag{S10}$$

where P_{in} represents the total incident power density from the solar spectrum and P_m denotes the maximum value of the output power density P. Shockley and Queisser (SQ) proposed a classic and universal efficiency estimation for solar cells, which only depends on the electronic band gap of the materials.[5] To improve the simplified SQ approximation, Yu and Zunger theoretically established the SLME method,[16,17] in which the power density P can be obtained from the product of the current density J and voltage V,

$$P = JV = [J_{sc} - J_0(exp(eV/k_BT) - 1]V, \tag{S11}$$

where T represents the temperature, J_{sc} denotes the short circuit current density, and J_0 is the reverse saturation current density, respectively. Both J_{sc} and J_0 can be calculated from the photon absorptivity $a(E)$ of the absorbers, the AM1.5G solar spectrum I_{sum}, and the blackbody spectrum $I_{bb}(E,T)$ as follows,

$$J_{sc} = e \int_0^\infty a(E)I_{sum}(E)dE, \tag{S12}$$

$$J_0 = \frac{J_0^r}{f_r} = \frac{e\pi}{f_r} \int_0^\infty a(E)I_{bb}(E,T)dE, \tag{S13}$$

where f_r is the fraction of the radiative recombination current and J_0^r denotes the radiative recombination current density.

1.6 PSC Device Model

To investigate the J-V characteristic and PCE in the PSC device, we adopt the wxAMPS code.[18,19] This code uses Newton and Gummel methods to solve the transport equations, which start from the Poisson's equation and the continuity equations for the electrons and holes,

$$\frac{d}{dx}(-\varepsilon(x)\frac{d\Psi}{dx}) = \rho, \tag{S14}$$

$$\frac{1}{q}\frac{dJ_n}{dx} = -G_{op}(x) + R(x), \tag{S15}$$

$$\frac{1}{q}\frac{dJ_p}{dx} = -G_{op}(x) - R(x), \tag{S16}$$

where ρ denotes total space charge density, Ψ labels the electrostatic potential, ε represents the permittivity, and q is the electron charge. The generation/recombination rate G/R, and the densities of electron/hole current J_n/J_p are functions of the position coordinate x. The charge density ρ is given by,

$$\rho = q[p(x) - n(x) + N_D^+(x) - N_A^-(x) + p_t(x) - n_t(x)], \tag{S17}$$

where n/p, n_t/p_t and N_D^+/N_A^- are free electron/hole density, trapped electron/hole density, and the ionized donor/acceptor-like doping concentration as a function of position x in the device.

2 Crystal structure and stability of $Ba_2X_2[Cs_{n-1}Sn_nX_{3n+1}]$ (X=I, Br, Cl; n=1, 2, 3)

Table S1 Calculated lattice parameters a, c (see the labels in Figure 1a) and distortion angle θ for $Ba_2X_2[Cs_{n-1}Sn_nX_{3n+1}]$ (X=I, Br, Cl; n=1, 2, 3), compared with RP perovskite $Cs_2[Cs_{n-1}Sn_nX_{3n+1}]$. Due to the imperfect match between perovskite layer and [Ba_2X_2] layer, the lattice parameter a of AV perovskites is slightly different from RP perovskites. For I-based perovskites, a_{AV} (6.070 Å) is smaller than a_{RP} (6.157 Å), indicating that the [Ba_2I_2] layer provides a compressive stress to the perovskite layer. On the contrary, a_{AV} of Cl-based AV perovskite (5.606 Å) is larger than a_{RP} (5.553 Å), indicating that [Ba_2Cl_2] layer provides a tensile stress for the perovskite layer. But for Br-based perovskites, the lattice parameter a of RP and AV perovskites are 5.804 and 5.838 Å, indicating that the perovskite layer matches the [Ba_2Br_2] layer well.

| Material	n	a (Å)	c (Å)	θ
$Ba_2I_2[Cs_{n-1}Sn_nI_{3n+1}]$	1	6.070	22.991	180°
	2	6.194	34.789	176.01°
	3	6.228	47.283	176.29°
$Ba_2Br_2[Cs_{n-1}Sn_nBr_{3n+1}]$	1	5.838	20.083	180°
	2	5.822	32.131	175.39°
	3	5.837	44.085	176.08°
$Ba_2Cl_2[Cs_{n-1}Sn_nCl_{3n+1}]$	1	5.606	18.686	180°
	2	5.528	30.833	172.88°
	3	5.557	42.298	174.80°
$Cs_2[Cs_{n-1}Sn_nI_{3n+1}]$	1	6.157	19.595	180°
$Cs_2[Cs_{n-1}Sn_nBr_{3n+1}]$	1	5.804	18.478	180°
$Cs_2[Cs_{n-1}Sn_nCl_{3n+1}]$	1	5.553	17.634	180°
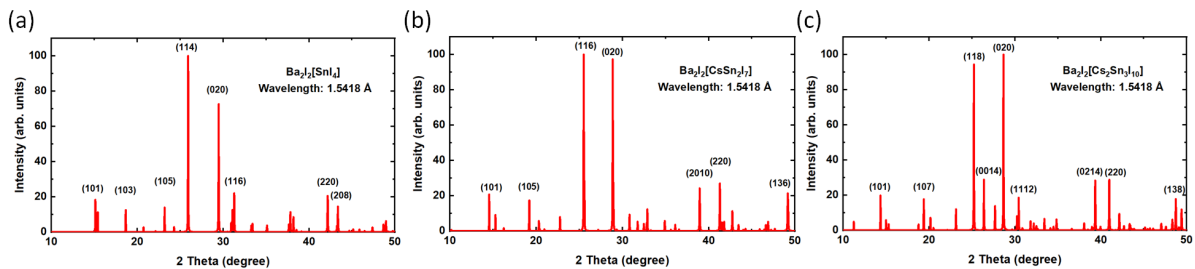
Figure S1 Calculated XRD pattern of bulk (a) $Ba_2I_2[SnI_4]$, (b) $Ba_2I_2[CsSn_2I_7]$ and (c) $Ba_2I_2[Cs_2Sn_3I_{10}]$. The radiation wavelength is chosen as 1.5418 Å (Cu $K\alpha$), and several important crystal faces are marked with corresponding Miller indices (hkl), where several crystal planes with $l \geq 10$ naturally become four-digit indices. All XRD patterns are calculated by using VESTA.[20]
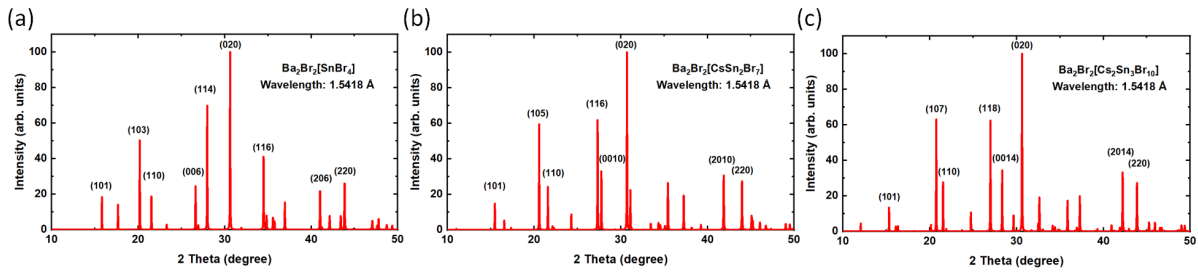
Figure S2 Calculated XRD pattern of bulk (a) $Ba_2Br_2[SnBr_4]$, (b) $Ba_2Br_2[CsSn_2Br_7]$ and (c) $Ba_2Br_2[Cs_2Sn_3Br_{10}]$. The radiation wavelength is chosen as 1.5418 Å (Cu $K\alpha$), and several important crystal faces are marked with corresponding Miller indices (hkl), where several crystal planes with $l \geq 10$ naturally become four-digit indices. All XRD patterns are calculated by using VESTA.[20]
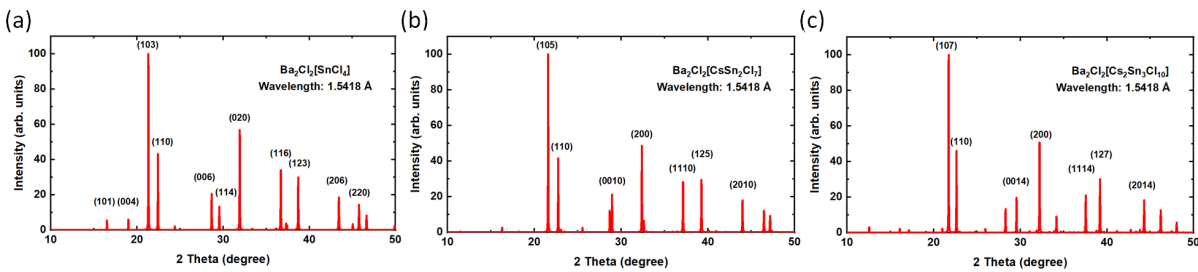
Figure S3 Calculated XRD pattern of bulk (a) $Ba_2Cl_2[SnCl_4]$, (b) $Ba_2Cl_2[CsSn_2Cl_7]$ and (c) $Ba_2Cl_2[Cs_2Sn_3Cl_{10}]$. The radiation wavelength is chosen as 1.5418 Å (Cu $K\alpha$), and several important crystal faces are marked with corresponding Miller indices (hkl), where several crystal planes with $l \geq 10$ naturally become four-digit indices. All XRD patterns are calculated by using VESTA.[20]
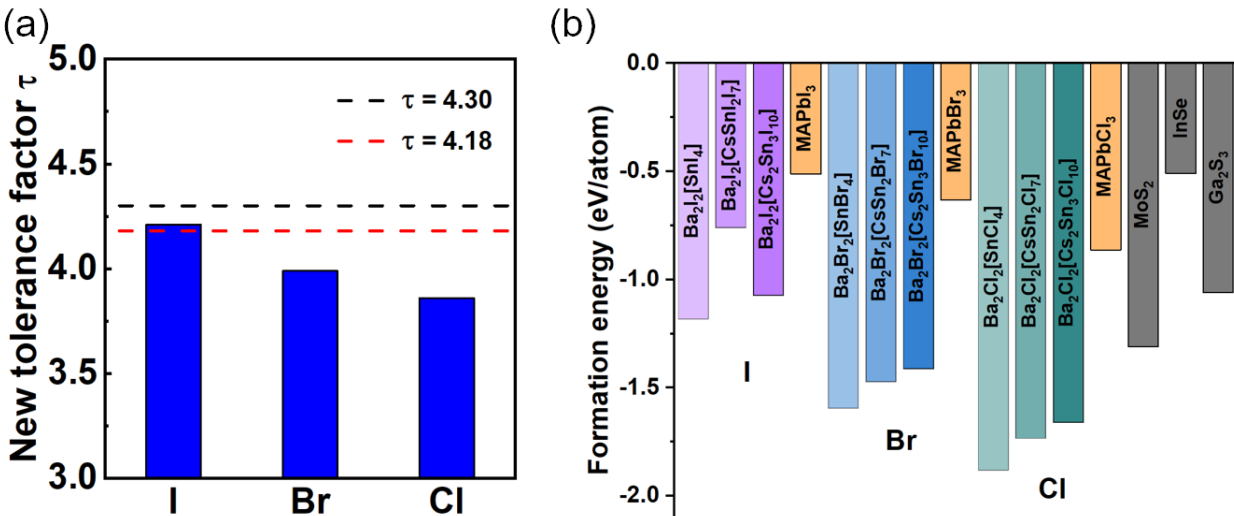
Figure S4 (a) The new tolerance factor τ for $Ba_2X_2[Cs_{n-1}Sn_nX_{3n+1}]$ (X=I, Br, Cl) perovskites. τ is calculated using the expression: $\tau = \frac{r_X}{r_B} - n_A(n_A - \frac{r_A/r_B}{ln(r_A/r_B)})$.[21] $\tau < 4.18$ indicates that the crystal is perovskite with a high overall accuracy of 92%, and there are a few perovskites existing with τ in the range of 4.18~4.30 as well.[21] (b) The calculated formation energy for $Ba_2X_2[Cs_{n-1}Sn_nX_{3n+1}]$ (X=I, Br, Cl; n=1, 2, 3), MAPbX$_3$ (X=I, Br, Cl), and several typical 2D semiconductors.
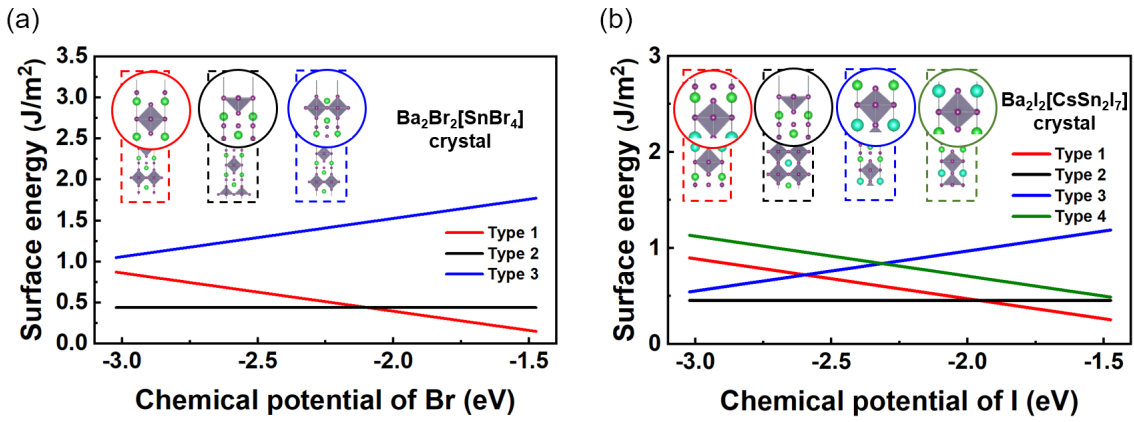
Figure S5 (a) Surface energy for three possible surface morphologies for $Ba_2Br_2[SnBr_4]$. (b) Surface energy for four possible surface morphologies for $Ba_2I_2[CsSn_2I_7]$. We did not choose to calculate the decomposition enthalpy in the oxidation reaction because the Sn^{2+} in Sn-based perovskites are easily oxidized, and the result of the decomposition enthalpy is often disappointing. On the contrary, the passivation and other techniques can be used to separate the material from oxygen and successfully prevent the oxidation reaction.[22] This process cannot be described by the decomposition enthalpy. In this work, we demonstrate that the $[Ba_2X_2]$ layer insulates oxygen, in which the surface energy is more effective than the decomposition enthalpy. Therefore, we focus on the isolation of oxygen by the $[Ba_2X_2]$ layer, not the oxidation reaction.

**Table S2** Elastic constants (GPa) of the AV-phase $Ba_2X_2[Cs_{n-1}Sn_nX_{3n+1}]$ perovskites (X= I, Br, Cl; n=1, 2, 3). The matrix of second-order elastic constants C_{44} decreases with increasing of the octahedral layer number n. Therefore, the accumulation of octahedral layers along the z axis unfortunately reduces the stability of $Ba_2X_2[Cs_{n-1}Sn_nX_{3n+1}]$, and potential distortion or slip may occur accordingly. For $Ba_2Cl_2[Cs_{n-1}Sn_nCl_{3n+1}]$ perovskites, the structure will become mechanically unstable when n≥3.

Material	C_{11}	C_{12}	C_{33}	C_{13}	C_{44}	C_{66}	
$Ba_2I_2[SnI_4]$	37.52	-0.74	14.38	10.32	4.40	1.27	stable
$Ba_2Br_2[SnBr_4]$	40.55	-4.45	19.98	15.31	3.70	0.46	stable
$Ba_2Cl_2[SnCl_4]$	49.61	-2.40	27.74	15.46	3.98	0.92	stable
$Ba_2I_2[CsSn_2I_7]$	31.72	4.37	19.68	10.47	2.35	2.36	stable
$Ba_2Br_2[CsSn_2Br_7]$	42.53	2.42	23.70	14.88	0.39	2.58	stable
$Ba_2Cl_2[CsSn_2Cl_7]$	40.55	-4.44	19.97	15.30	3.69	0.45	stable
$Ba_2I_2[Cs_2Sn_3I_{10}]$	31.44	5.17	21.16	8.65	2.02	2.96	stable
$Ba_2Br_2[Cs_2Sn_3Br_{10}]$	42.51	4.09	22.62	11.96	0.17	3.41	stable
$Ba_2Cl_2[Cs_2Sn_3Cl_{10}]$	48.52	5.28	21.17	13.23	-3.65	4.31	unstable

3 Accurate band structures and band gaps of $Ba_2X_2[Cs_{n-1}Sn_nX_{3n+1}]$
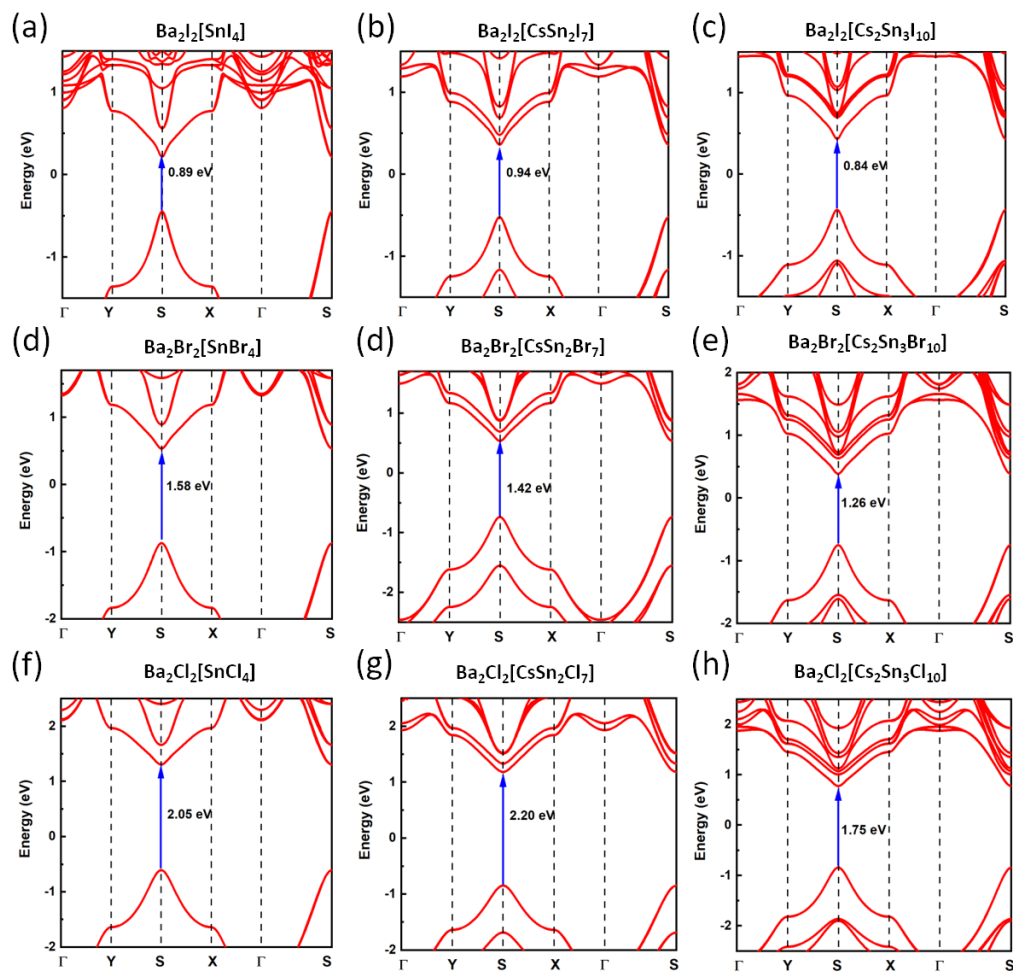
Figure S6 The calculated electronic band structures of $Ba_2X_2[Cs_{n-1}Sn_nX_{3n+1}]$ (X= I, Br, Cl; n=1, 2, 3) in which the SOC effect is included.
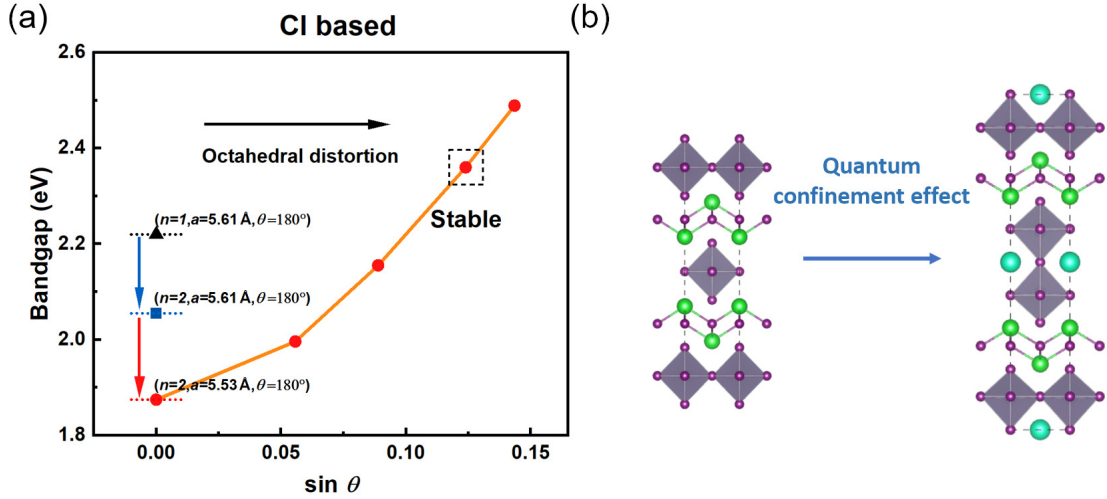
Figure S7 (a) The changes of band gaps for $Ba_2Cl_2[Cs_{n-1}Sn_nCl_{3n+1}]$ (n=1, 2). (b) The quantum confinement effect, which will be weakened with the thickening perovskite-like sheet.

4 The SOC effect analysis by the $k \cdot p$ method

Table S3 The parameters of the effective Hamiltonian

P_x	P_y	K_{xy}	L_1	N_1	M_2	λ
41.86	46.99	444.89	-244.41	683.36	176.48	0.24

The conduction band shift can be quantificationally described by the energy eigenvalues of three conduction band states at S point. To simplify the expressions, we approximate energy levels of $|X\rangle$ and $|Y\rangle$ equal, which in fact are only 0.03 eV apart. For three conduction bands, the energy eigenvalues are given as,

$$\begin{cases} E_{cbm} = \frac{a}{3} - \frac{\sqrt{b}}{6}\cos(\arctan(\frac{\sqrt{4b^3-c^2}}{c}) + \pi), \\ E_{cbm+1} = \frac{a}{3} - \frac{\sqrt{b}}{6}\cos(\arctan(\frac{\sqrt{4b^3-c^2}}{c}) - \pi), \\ E_{cbm+2} = \frac{a}{3} + \frac{\sqrt{b}}{6}\cos(\arctan(\frac{\sqrt{4b^3-c^2}}{c})), \end{cases} \tag{S18}$$

where,

$$\begin{cases} a = E_{cbm,0} + E_{cbm+1,0} + E_{cbm+2,0}, \\ b = 8((\delta_{01})^2 + (\delta_{12})^2 + (\delta_{20})^2) + 36\lambda^2, \\ c = \frac{64}{3}((\delta_{01} - \delta_{12})^3 + (\delta_{12} - \delta_{20})^3 + (\delta_{20} - \delta_{12})^3) + 432\lambda^3. \end{cases} \tag{S19}$$

In these expressions, $E_{cbm,0}$, $E_{cbm+1,0}$, $E_{cbm+2,0}$ are the energy eigenvalues of $|X\rangle$, $|Y\rangle$, $|Z\rangle$ at S point ($E_{cbm,0} \approx E_{cbm+1,0} < E_{cbm+2,0}$) without the SOC effect, λ is the SOC strength, $\delta_{01} = E_{cbm,0} - E_{cbm+1,0}$, $\delta_{12} = E_{cbm+1,0} - E_{cbm+2,0}$ and $\delta_{20} = E_{cbm+2,0} - E_{cbm,0}$.

In order to analyze the influence of the SOC effect on band dispersion, we next give the expression of E_{cbm} in the neighborhood of CBM. We only discuss the case along $S - \Gamma$ path, in which E_{cbm} only depends on k_x. E_{cbm} can be expressed as a Taylor series expansion of k_x,

$$E_{cbm} = \frac{a}{3} - \frac{\sqrt{b}}{6}\cos(\arctan(\frac{\sqrt{4b^3-c^2}-\pi}{c})) + \frac{p_x^2 k_x^2}{2}(F(\lambda, E_g)) + O(k_x^4), \tag{S20}$$

where the band gap $E_g = E_{cbm} - E_{vbm}$ and $F(\lambda, E_g)$ is a complex function of λ and E_g. As we ignore the higher order of k_x ($O(k_x^4)$), E_{cbm} is thus parabolic function of k_x near the band edge, in which the dispersion is positively related to the

quadratic coefficient. Because λ is relative small ($\sim$0.24 eV) compared with E_g, we could take the first order approximation to the quadratic coefficient as follows,

$$a_2 = \frac{p_x^2 k_x^2}{2E_g}(1 + \frac{\lambda}{2E_g}), \tag{S21}$$

which shows that the SOC effect increases the quadratic coefficient and makes CBM much more dispersive.

5 Optical absorption, SLME, J-V curve and the parameters of wx-AMPS simulation

Table S4 Calculated values of the reduced effective mass μ^*, high-frequency dielectric constant ε_∞ and exciton binding energy E_b for $Ba_2X_2[Cs_{n-1}Sn_nX_{3n+1}]$ (X=I, Br, Cl; n=1, 2, 3). The exciton binding energy is calculated using the expression $E_b = \mu^*/\varepsilon_\infty^2 \times E_{Ry}$ eV.[23]

Material	μ^* (m_0)	ε_∞	E_b (meV)
$Ba_2I_2[SnI_4]$	0.04	6.7	11
$Ba_2Br_2[SnBr_4]$	0.07	5.3	34
$Ba_2Cl_2[SnCl_4]$	0.10	4.5	65
$Ba_2I_2[CsSn_2I_7]$	0.06	7.0	16
$Ba_2Br_2[CsSn_2Br_7]$	0.08	5.4	36
$Ba_2Cl_2[CsSn_2Cl_7]$	0.15	4.3	113
$Ba_2I_2[Cs_2Sn_3I_{10}]$	0.05	6.9	13
$Ba_2Br_2[Cs_2Sn_3Br_{10}]$	0.07	5.3	32
$Ba_2Cl_2[Cs_2Sn_3Cl_{10}]$	0.10	4.2	75
MAPbI$_3$ [23]	0.06	5.8	44
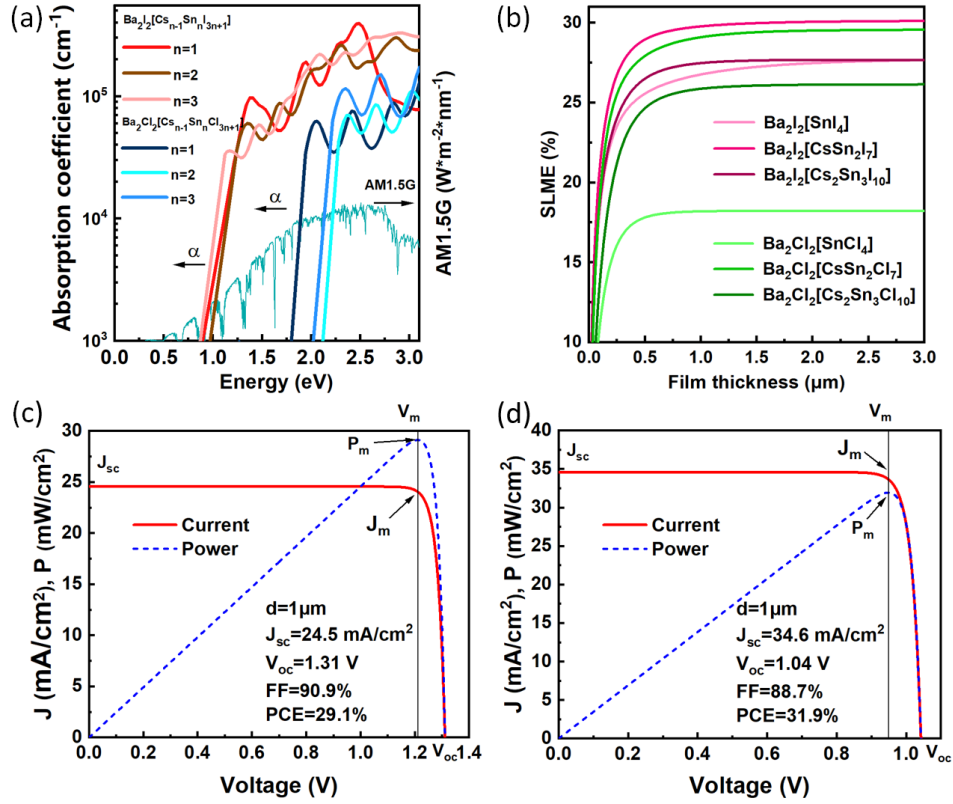
Figure S8 (a) Interband optical absorption spectra of $Ba_2I_2[Cs_{n-1}Sn_nI_{3n+1}]$ (red lines) and $Ba_2Cl_2[Cs_{n-1}Sn_nCl_{3n+1}]$, along with Air Mass (AM) 1.5G Spectra.[24] (b) Estimated SLME of $Ba_2X_2[Cs_{n-1}Sn_nX_{3n+1}]$ (X=Cl and I). Calculated J-V characteristic of (c) $Ba_2Br_2[SnBr_4]$ and (d) $Ba_2Br_2[CsSn_2Br_7]$ at a thickness of 1 μm.

Table S5 The input parameters of wxAMPS simulation for $Ba_2Br_2[Cs_2Sn_3Br_{10}]$ PSC. The parameters of SnO_2 and $CuSbS_2$ are taken from ref.[25–27]

Parameters	SnO_2	$Ba_2Br_2[Cs_2Sn_3Br_{10}]$	$CuSbS_2$
Thickness (μm)	0.05	0.50	0.05
Permittiviy	9	35	8.2
Band gap (eV)	3.6	1.26	1.58
Affinity (eV)	4.6	4.6	4.2
N_c (cm^{-3})	2.2×10^{18}	1.33×10^{18}	2×10^{18}
N_v (cm^{-3})	1.8×10^{19}	1.06×10^{18}	1×10^{19}
μ_e (cm^2/(v·s))	100	135	49
μ_h (cm^2/(v·s))	0.256	173	49
N_d (cm^{-3})	1×10^{17}	0	0
N_a (cm^{-3})	0	2.1×10^{17}	1.38×10^{18}

Notes and references

[1] G. Kresse and J. Furthmüller, *Comput. Mater. Sci.*, 1996, **6**, 15–50.

[2] G. Kresse and J. Furthmüller, *Phys. Rev. B*, 1996, **54**, 11169–11186.

[3] P. E. Blöchl, *Phys. Rev. B*, 1994, **50**, 17953–17979.

[4] J. P. Perdew, K. Burke and M. Ernzerhof, *Phys. Rev. Lett.*, 1996, **77**, 3865–3868.

[5] H. J. Monkhorst and J. D. Pack, *Phys. Rev. B*, 1976, **13**, 5188–5192.

[6] A. V. Krukau, O. A. Vydrov, A. F. Izmaylov and G. E. Scuseria, *J. Chem. Phys.*, 2006, **125**, 224106.

[7] E. O. Kane, *J. Phys. Chem. Solids*, 1957, **1**, 249–261.

[8] R. P. Feynman, *Phys. Rev.*, 1955, **97**, 660–665.

[9] R. P. Feynman, R. W. Hellwarth, C. K. Iddings and P. M. Platzman, *Phys. Rev.*, 1962, **127**, 1004–1017.

[10] M. Sendner, P. K. Nayak, D. A. Egger, S. Beck, C. Müller, B. Epding, W. Kowalsky, L. Kronik, H. J. Snaith, A. Pucci and R. Lovrinčić, *Mater. Horiz.*, 2016, **3**, 613–620.

[11] I. Biaggio, R. W. Hellwarth and J. P. Partanen, *Phys. Rev. Lett.*, 1997, **78**, 891–894.

[12] H. Fröhlich, *Adv. Phys.*, 1954, **3**, 325–361.

[13] S. Saha, T. P. Sinha and A. Mookerjee, *Phys. Rev. B*, 2000, **62**, 8828–8834.

[14] A. Moscowitz, in *Theoretical Aspects of Optical Activity Part One: Small Molecules*, John Wiley Sons, Ltd, 1962, pp. 67–112.

[15] S. Saha, T. P. Sinha and A. Mookerjee, *Phys. Rev. B*, 2000, **62**, 8828–8834.

[16] L. Yu and A. Zunger, *Phys. Rev. Lett.*, 2012, **108**, 068701.

[17] L. Yu, R. S. Kokenyesi, D. A. Keszler and A. Zunger, *Adv. Energy Mater.*, 2013, **3**, 43–48.

[18] Y. Liu, Y. Sun and A. Rockett, *Sol. Energy Mater. Sol. Cells*, 2012, **98**, 124–128.

[19] H. Zhu, A. K. Kalkan, J. Hou and S. J. Fonash, *AIP Conf. Proc.*, 1999, **462**, 309–314.

[20] K. Momma and F. Izumi, *J. Appl. Crystallogr.*, 2011, **44**, 1272–1276.

[21] C. J. Bartel, C. Sutton, B. R. Goldsmith, R. Ouyang, C. B. Musgrave, L. M. Ghiringhelli and M. Scheffler, *Science Advances*, 2019, **5**, eaav0693.

[22] X. Liu, Y. Wang, T. Wu, X. He, X. Meng, J. Barbaud, H. Chen, H. Segawa, X. Yang and L. Han, *Nat. Commun.*, 2020, **11**, 2678.

[23] M. R. Filip, G. E. Eperon, H. J. Snaith and F. Giustino, *Nat. Commun.*, 2014, **5**, 5757.

[24] *Air Mass 1.5 Spectra*, `https://www.nrel.gov/grid/solar-resource/spectra-am1.5.html`, Accessed June 17, 2021.

[25] S. Rai, B. Pandey, A. Garg and D. Dwivedi, *Opt. Mater.*, 2021, **121**, 111645.

[26] M. Ye, C. He, J. Iocozzia, X. Liu, X. Cui, X. Meng, M. Rager, X. Hong, X. Liu and Z. Lin, *J. Phys. D: Appl. Phys.*, 2017, **50**, 373002.

[27] F. Wang, Y. Cao, C. Chen, Q. Chen, X. Wu, X. Li, T. Qin and W. Huang, *Adv. Funct. Mater.*, 2018, **28**, 1803753.